

Effects of the QCD critical point on the spectra and flow coefficients of hadrons

Sushant K. Singh^{*} and Jan-e Alam

*Variable Energy Cyclotron Centre, 1/AF, Bidhan Nagar, Kolkata, India
and HBNI, Training School Complex, Anushakti Nagar, Mumbai 400085, India*

 (Received 28 May 2022; accepted 11 April 2023; published 28 April 2023)

The space-time evolution of the hot and dense fireball of quarks and gluons produced in ultrarelativistic heavy-ion collisions at nonzero baryonic chemical potential and temperature has been studied by using relativistic dissipative hydrodynamics. For this purpose, a numerical code has been developed to solve the relativistic viscous causal hydrodynamics in $(3 + 1)$ dimensions with the inclusion of QCD critical point (CP) through the equation of state and scaling behavior of transport coefficients. We compute the transverse momentum spectra, directed and elliptic flow coefficients of pions and protons to comprehend the effect of CP on these observables. It is found that the integration over the entire space-time history of the fireball largely obliterates the effects of CP on the spectra and flow coefficients for the event averaged initial conditions considered here.

DOI: [10.1103/PhysRevD.107.074042](https://doi.org/10.1103/PhysRevD.107.074042)

I. INTRODUCTION

Calculations based on lattice QCD and effective field theoretical models at nonzero temperature (T) and baryon chemical potential (μ_B) affirm a complex phase diagram [1–6] (see Ref. [7] for a contemporary review). It is established by lattice QCD calculations that at high T and low μ_B ($\rightarrow 0$) the quark-hadron transition is a crossover. However, the transition may be first order in nature [5,8] at low T and high μ_B . Therefore, it is expected that between the crossover and the first-order transition there may exist a point in the $\mu_B - T$ plane, called the critical end point or simply critical point (CP) where the first-order transition ends and the crossover begins [9]. The location of the CP is not yet precisely known from lattice QCD based calculations [10] due to the well-known sign problem for spin-1/2 particle (quark) [11] at nonzero μ_B .

However, there are several calculations based on effective field theoretic models at nonzero baryon density [12–15] predicting diverse locations for the CP in the $\mu_B - T$ plane [16]. The coordinates of the CP , (μ_{Bc}, T_c) , depend on the values of the parameters of the model. In the present work, we take $(\mu_{Bc}, T_c) = (350 \text{ MeV}, 143.2 \text{ MeV})$ as a representing point for CP in the QCD phase diagram. Experimental observables do not carry information of a single point in the $\mu_B - T$ plane of the QCD but superposition of all the points that the trajectory experiences from the initial state to the final freeze-out. Therefore, it is expected that the imprint of the CP will be stronger if it is located near

the freeze-out boundary. Moreover, the size and shape of the critical region may affect the observables [17].

It is generally accepted that the quark gluon plasma (QGP) system formed with small μ_B and high T in nuclear collisions at top Relativistic Heavy Ion Collider (RHIC) and Large Hadron Collider (LHC) energies reverts to hadronic phase via crossover transition. The ongoing Beam Energy Scan (BES-II) program at RHIC, the upcoming Compressed Baryonic Matter, and the Nuclotron Based Ion Collider Facility experiments are projected to produce QGP at higher μ_B and lower T , which revert to the hadronic phase through a first-order phase transition. The QCD matter at different values of T and μ_B can be produced in nuclear collisions by regulating the center-of-mass energy per nucleon ($\sqrt{s_{NN}}$) of the colliding nuclei and scanning through different rapidities at a given colliding energy. Therefore, the colliding energy and the rapidity (y) bin should judiciously be chosen to approach the critical point at (μ_{Bc}, T_c) .

Several signatures of the CP have been proposed in the literature. An early work [18] predicts that the existence of the CP will be associated with large event-by-event fluctuations of low momentum pions and suppressed fluctuations in T and μ_B . It has been shown in Ref. [17] that the CP produces a peak in the kurtosis of the net proton and creates lensing effects [19] on the hydrodynamic trajectories subsequently influencing the kurtosis. The nonmonotonic dependence of multiplicity fluctuations on $\sqrt{s_{NN}}$ [20], the y dependence of cumulants of the event-by-event proton distributions [21] and the multiplicity fluctuations of pions and protons [22], and the appearance of negative kurtosis of the order parameter fluctuation [23] are some of the proposed signals of the CP (for a review, see Ref. [24] and references therein).

^{*}Corresponding author.
sushant7557@gmail.com

Relativistic hydrodynamics (see Refs. [25,26] for review and references therein) has been used extensively to analyze various experimental data originating from heavy-ion collisions over a wide range of $\sqrt{s_{NN}}$ to extract properties of the hot and dense QCD matter. It will be interesting to study how the hydrodynamic evolution of the QCD matter will be affected by the presence of CP . The effects of CP enter into the relativistic viscous hydrodynamics through the equation of state (EOS) and transport coefficients. The CP changes the EOS and various transport coefficients drastically. Therefore, it will be useful to examine the effects of CP on some of the observables, i.e., the transverse momentum (p_T) distribution of the hadrons and the p_T and y dependence of flow coefficients.

We will use relativistic viscous causal hydrodynamics of Israel and Stewart [27] with EOS containing the effect of CP and the scaling behavior of shear and bulk viscosities near the CP . In a recent study, we have found that the CP has the potential to substantially alter the spin polarization of hadrons [28]. In the present work, we will investigate the response of the p_T and y distributions and directed and elliptic flow coefficients of hadrons (proton and pion) to the QCD critical point.

For this exercise, a numerical code in FORTRAN has been developed to solve (3 + 1)-dimensional viscous relativistic causal hydrodynamics using the algorithm detailed in Ref. [29]. The code includes the effect of CP through the EOS and the scaling behavior of the transport coefficients. The subroutines used for the initial condition and the EOS to solve hydrodynamic equations have been extensively tested by reproducing the results available in Refs. [30,31], respectively. The CORNELIUS code [32] has been used to find the freeze-out hypersurface characterized by constant energy density. The results from the code without CP have been contrasted with the known analytical results of Ref. [33] and numerical results from the codes AZHYDRO [34], MUSIC [35], and VHLE [29].

The objective of the present work is to apply the tools that we develop to study the effects of CP on hadronic spectra and flow coefficients and find out whether these quantities carry any observable imprints of the CP .

The paper is organized as follows. In Sec. II, the method for the numerical solution of hydrodynamic equations is discussed. Relevant inputs, e.g., the initial condition, EOS, and transport coefficients, are presented through different subsections of this section. We present the results in Secs. III and IV is devoted to summary and discussions.

II. NUMERICAL SOLUTION OF RELATIVISTIC HYDRODYNAMICS

Throughout the paper, we use natural units with $c = \hbar = k_B = 1$ where c is the speed of light in vacuum, $\hbar (=2\pi\hbar)$ is the Planck constant, and k_B is the Boltzmann constant. The flat space-time metric is taken as $g_{\mu\nu} = \text{diag}(1, -1, -1, -1)$.

A. Hydrodynamic equations

The relativistic hydrodynamic equations governing the evolution of the system are

$$\begin{aligned}\partial_\mu T^{\mu\nu} &= 0, \\ \partial_\mu J_B^\mu &= 0,\end{aligned}\quad (1)$$

where $T^{\mu\nu}$ is the energy-momentum tensor and J_B^μ is the net-baryon number current. In the Landau frame of reference, $T^{\mu\nu}$ and J_B^μ are given by

$$T^{\mu\nu} = \varepsilon u^\mu u^\nu - (P + \Pi)\Delta^{\mu\nu} + \pi^{\mu\nu}, \quad (2)$$

$$J_B^\mu = n_B u^\mu + V^\mu, \quad (3)$$

where ε , n_B , P , u^μ , Π , $\pi^{\mu\nu}$, V^μ , and $\Delta^{\mu\nu} (=g^{\mu\nu} - u^\mu u^\nu)$ denote, respectively, the energy density, net-baryon number density, thermodynamic pressure, 4-velocity, bulk pressure, shear-stress tensor, baryon diffusion 4-current, and projector tensor onto the space orthogonal to u^μ . We take $V^\mu = 0$ in the present study. In the Israel-Stewart framework, the viscous terms obey relaxation-type equations, which are taken as [29]

$$u^\gamma \partial_\gamma \Pi = -\frac{\Pi - \Pi_{NS}}{\tau_\Pi} - \frac{4}{3} \Pi \partial_\gamma u^\gamma, \quad (4)$$

$$\langle u^\gamma \partial_\gamma \pi^{\mu\nu} \rangle = -\frac{\pi^{\mu\nu} - \pi_{NS}^{\mu\nu}}{\tau_\pi} - \frac{4}{3} \pi^{\mu\nu} \partial_\gamma u^\gamma, \quad (5)$$

where $\langle \cdot \rangle$ is defined as

$$\langle A^{\mu\nu} \rangle = \left(\frac{1}{2} \Delta_\alpha^\mu \Delta_\beta^\nu + \frac{1}{2} \Delta_\nu^\alpha \Delta_\beta^\mu - \frac{1}{3} \Delta^{\mu\nu} \Delta_{\alpha\beta} \right) A^{\alpha\beta} \quad (6)$$

and Π_{NS} , $\pi_{NS}^{\mu\nu}$ are the Navier-Stokes limit of Π and $\pi^{\mu\nu}$, respectively, and are given by

$$\Pi_{NS} = -\zeta\theta, \quad (7)$$

$$\pi_{NS}^{\mu\nu} = 2\eta\langle\partial^\alpha u^\beta\rangle. \quad (8)$$

The transport coefficients are positive, i.e., $\eta, \zeta > 0$, where η and ζ are the shear viscosity and bulk viscosity, respectively. As mentioned above, a numerical code has been developed in FORTRAN programming language to solve the hydrodynamic equations in Milne coordinates (τ, x, y, η_s) , using the relativistic HLLE algorithm as in Ref. [29], where $\tau = \sqrt{t^2 - z^2}$ and $\eta_s = \tanh^{-1}(z/t)$. The various inputs to the numerical program needed for this study are detailed below.

B. Initial condition

In this work, we have used the event-averaged initial condition for energy density and baryon density, and all the dissipative fluxes are initialized to their corresponding Navier-Stokes limit. The Glauber model is used to estimate the energy density profile at the initial time, τ_0 , required to solve the hydrodynamical equations. The value of τ_0 , for the hydrodynamic simulation, is assumed as the time taken by the two colliding nuclei to pass through one another for $\sqrt{s_{NN}} \leq 40$ GeV, which is determined by the expression

$$\tau_0 \approx \frac{2R}{\gamma_z v_z}, \quad (9)$$

where $\gamma_z = \frac{1}{\sqrt{1-v_z^2}}$ and $v_z = \tanh(y_b)$, with $y_b = \cosh^{-1}(\sqrt{s}/2m_N)$ as the beam rapidity; m_N is the mass of a nucleon; and R is the radius of nucleus. The value of τ_0 is taken as 1 fm/c for $\sqrt{s_{NN}} > 40$ GeV.

The inelastic nucleon-nucleon cross section (σ_{NN}^{in}) required as an input to the Glauber model as a function of the colliding energy \sqrt{s} (in GeV) is taken from the following parametrization [36,37]:

$$\begin{aligned} \sigma_{NN}^{\text{tot}}(\sqrt{s}) &= 42.6s^{-0.46} - 33.4s^{-0.545} + 35.5 \\ &\quad + 0.307\ln^2(s/29.1), \\ \sigma_{NN}^{\text{el}}(\sqrt{s}) &= 5.17 + 12.99s^{-0.41} + 0.09\ln^2(s/29.2), \\ \sigma_{NN}^{\text{in}}(\sqrt{s}) &= \sigma_{NN}^{\text{tot}} - \sigma_{NN}^{\text{el}}. \end{aligned} \quad (10)$$

Our model for the initial condition is based on the inputs taken from Refs. [30,38]. The collision axis is assumed to be along the z axis. Let n_A and n_B denote the number of wounded nucleons per unit area in the transverse plane of the two colliding nuclei A and B , respectively moving along the positive and negative z axis. The n_A (n_B) is given by

$$n_{A,B} = T_{A,B} \left[1 - \left(1 - \frac{\sigma_{NN}^{\text{in}} T_{B,A}}{N_{B,A}} \right)^{N_{B,A}} \right], \quad (11)$$

where N_A and N_B denote the total number of nucleons in A and B , respectively, and the thickness functions $T_A(x, y)$ and $T_B(x, y)$ are calculated as

$$T_{A,B}(x, y) = \int_{-\infty}^{\infty} \varrho_{A,B}(x, y, z') dz', \quad (12)$$

where $\varrho_{A,B}(x, y, z)$ is the nuclear density profile assumed to have the Woods-Saxon shape,

$$\varrho_{A,B}(x, y, z) = \frac{\varrho_0}{1 + e^{-\frac{r-R(\theta)}{\delta}}}. \quad (13)$$

The constant ϱ_0 is chosen to satisfy the relation

$$\int \varrho_i(\vec{r}) d^3\vec{r} = N_i, \quad i = A, B, \quad (14)$$

and $R(\theta)$ has been taken as a function of the polar angle, θ , to account for any deformation of the nucleus and is given by

$$R(\theta) = R_0[1 + \beta_2 Y_{2,0}(\theta) + \beta_4 Y_{4,0}(\theta)], \quad (15)$$

where $Y_{l,m}(\theta, \phi)$ denotes the spherical harmonics. In this study, we consider nuclei to be spherical and take $\beta_2, \beta_4 = 0$. For gold (Au) nucleus, R_0 is taken as 6.37 fm. The initial energy density is assumed to have the form

$$\varepsilon(x, y, \eta_s; \tau_0) = e(x, y)f(\eta_s), \quad (16)$$

where $f(\eta_s)$ is given by [30]

$$f(\eta_s) = \exp \left[-\frac{(|\eta_s - y_{\text{CM}}| - \eta_0)^2}{2\sigma_\eta^2} \theta(|\eta_s - y_{\text{CM}}| - \eta_0) \right], \quad (17)$$

where y_{CM} is defined as

$$y_{\text{CM}} = \text{arctanh} \left[\frac{n_A - n_B}{n_A + n_B} \tanh(y_b) \right], \quad (18)$$

and $e(x, y) = \mathcal{N}_e M(x, y)$ with

$$M(x, y) = m_N \sqrt{n_A^2 + n_B^2 + 2n_A n_B \cosh(2y_b)}. \quad (19)$$

The normalization constant \mathcal{N}_e is determined by demanding local energy-momentum conservation [30]. It is also shown in Ref. [30] that such a choice is able to explain the experimental data on charged particle multiplicity and directed and elliptic flow for RHIC-BES collision energies. These collision energies overlap with the interest of the present work. Therefore, the model used in Ref. [30] may be considered suitable for the present purpose. Moreover, it may be important to mention here that the data on spin polarization and bulk observables can be simultaneously reproduced by using such initial conditions [39]. The following profile for the initial velocity distribution is assumed:

$$u^\mu(x, y, \eta_s) = (\cosh(\eta_s), 0, 0, \sinh(\eta_s)). \quad (20)$$

The assumption for the profile of u^μ puts a constraint on the normalization factor \mathcal{N}_e , making it a function of transverse coordinates, x and y . We take the profile for the initial baryon density

$$n_B(x, y, \eta_s; \tau_0) = \mathcal{N}_B [g_A(\eta_s)n_A(x, y) + g_B(\eta_s)n_B(x, y)], \quad (21)$$

where $g_A(\eta_s)$ and $g_B(\eta_s)$ are given by [38]

$$g_A(\eta_s) = \theta(\eta_s - \eta_{B,0}) \exp \left[-\frac{(\eta_s - \eta_{B,0})^2}{2\sigma_{B,\text{out}}^2} \right] + \theta(\eta_{B,0} - \eta_s) \times \exp \left[-\frac{(\eta_s - \eta_{B,0})^2}{2\sigma_{B,\text{in}}^2} \right], \quad (22)$$

$$g_B(\eta_s) = \theta(\eta_s + \eta_{B,0}) \exp \left[-\frac{(\eta_s + \eta_{B,0})^2}{2\sigma_{B,\text{in}}^2} \right] + \theta(-\eta_{B,0} - \eta_s) \times \exp \left[-\frac{(\eta_s + \eta_{B,0})^2}{2\sigma_{B,\text{out}}^2} \right]. \quad (23)$$

For the initial 4-velocity given in Eq. (20), the η_s component of the flow velocity is zero in Milne coordinates, i.e., $w^\mu = (1, 0, 0, 0)$; therefore, the normalization \mathcal{N}_B can be fixed by using the expression

$$\int \tau_0 dx dy d\eta_s n_B(x, y, \eta_s; \tau_0) = N_{\text{part}}, \quad (24)$$

$$\Rightarrow \int d\eta_s n_B(x, y, \eta_s; \tau_0) = \frac{1}{\tau_0} [n_A(x, y) + n_B(x, y)], \quad (25)$$

which gives

$$\mathcal{N}_B = \frac{1}{\tau_0} \sqrt{\frac{2}{\pi \sigma_{B,\text{in}} + \sigma_{B,\text{out}}}}. \quad (26)$$

The initial condition, hence, is modeled through six parameters $(\tau_0, \eta_0, \sigma_\eta, \eta_{B,0}, \sigma_{B,\text{in}}, \sigma_{B,\text{out}})$, which are chosen from Ref. [30] for Au + Au collisions. The value of impact parameter is chosen as 5 fm here, representing collisions which are neither too central with vanishing elliptic flow nor too peripheral to make thermalization questionable. However, any other value of b can also be chosen.

C. Equation of state

The EOS has been obtained by following the procedure detailed in Ref. [31] by assuming that the CP in QCD belongs to the same universality class as that of three-dimensional (3D) Ising model. The procedure is briefly reviewed below. The pressure at nonzero T and μ_B can be obtained through a Taylor series expansion about $\mu_B = 0$ as

$$P_{\text{QCD}}(T, \mu_B) = T^4 \sum_n c_{2n}(T) \left(\frac{\mu_B}{T} \right)^{2n}, \quad (27)$$

where

$$c_n(T) = \frac{1}{n!} \left. \frac{\partial^n (P/T^4)}{\partial (\mu_B/T)^n} \right|_{\mu_B=0} = \frac{1}{n!} \chi_n(T). \quad (28)$$

If there were no singularity, then the series expansion given in Eq. (27) would have been valid throughout the QCD phase diagram. However, the presence of CP makes some of the coefficients diverge. Hence, the pressure can be written as a sum of a regular and a singular part. Equivalently, the expansion coefficients in Eq. (27) are replaced by

$$T^4 c_n(T) \rightarrow T^4 c_n^{\text{Non-Ising}}(T) + f(T, \mu_B) c_n^{\text{Ising}}(T), \quad (29)$$

where the superscripts “Non-Ising” and “Ising” represent the regular and the singular (or critical) contributions respectively. $f(T, \mu_B)$ is chosen so that it does not add any other singularity in the problem and can simply be

$$f(T, \mu_B) = T_c^4. \quad (30)$$

The critical part is obtained by using the 3D Ising model because the QCD critical point belongs to the same universality class as the 3D Ising model. Hence, the two models must show the same scaling behavior in the critical region. The critical exponents of the 3D Ising model are known through numerical simulations. Hence, by mapping the parameters of the two systems in the critical region, it is possible to extract the critical behavior of QCD near T_c . The mapping from the Ising model phase diagram (r, h) to the QCD phase diagram (μ_B, T) is done with the help of the relations [31]

$$\begin{aligned} \frac{T - T_c}{T_c} &= w(r\rho \sin \alpha_1 + h \sin \alpha_2), \\ \frac{\mu_B - \mu_{BC}}{T_c} &= w(-r\rho \cos \alpha_1 - h \cos \alpha_2), \end{aligned} \quad (31)$$

where α_1 (α_2) is the angle between the horizontal axis for constant T and the $h = 0$ ($r = 0$) Ising model axis. w and ρ determine the overall and relative scale between r and h , respectively. The size and shape of the critical domain in the $\mu_B - T$ plane depend on the values of these mapping parameters. For the present study, we have used $w = 1$, $\rho = 2$, $\alpha_1 = 3.85^\circ$, and $\alpha_2 = 90^\circ - \alpha_1$.

The Ising pressure in the critical region is given by

$$P_{\text{Ising}}(R, \theta) = h_0 M_0 R^{2-\alpha} [\theta \tilde{h}(\theta) - g(\theta)], \quad (32)$$

where $\tilde{h}(\theta) = \theta(1 + a\theta^2 + b\theta^4)$ and $g(\theta) = c_0 + c_1(1 - \theta^2) + c_2(1 - \theta^2)^2 + c_3(1 - \theta^2)^3$; $h_0, M_0, a, b, c_0, c_1, c_2$, and c_3 are constants, some given in terms of critical exponents. The numerical values of these constants are same as in Ref. [31]. (R, θ) are related to (r, h) through the transformations

$$h = h_0 R^{\beta\delta} \tilde{h}(\theta), \quad (33)$$

$$r = R(1 - \theta^2), \quad (34)$$

where β and δ are critical exponents. Hence, the coefficients contributing to the critical part are determined through

$$c_n^{\text{Ising}}(T) = \frac{1}{n!} T^n \left. \frac{\partial^n P^{\text{Ising}}}{\partial \mu_B^n} \right|_{\mu_B=0}. \quad (35)$$

The Non-Ising coefficients are chosen in such a way that at $\mu_B = 0$ the expansion coefficients must match the results obtained from lattice QCD, i.e.,

$$T^4 c_n^{\text{LAT}}(T) = T^4 c_n^{\text{Non-Ising}}(T) + f(T, \mu_B = 0) c_n^{\text{Ising}}(T). \quad (36)$$

Having determined the Ising and Non-Ising coefficients, the full pressure is then obtained as

$$P_{\text{QCD}}(T, \mu_B) = T^4 \sum_n c_{2n}^{\text{Non-Ising}}(T) \left(\frac{\mu_B}{T} \right)^{2n} + T_c^4 P^{\text{Ising}}(R(T, \mu_B), \theta(T, \mu_B)). \quad (37)$$

The procedure as detailed above gives various thermodynamic observables as a function of T and μ_B . However, for our numerical hydrodynamic code, we require pressure (P) as a function of energy density (ε) and baryon number density (n_B). To construct such a table, we follow a procedure similar to that in Ref. [40]. The $\varepsilon - n_B$ plane is discretized with the following scheme:

$$\Delta\varepsilon(\text{GeV}/\text{fm}^3) = \begin{cases} 0.002 & \text{if } 0.001 \leq \varepsilon < 1.001, \\ 0.02 & \text{if } 1.001 \leq \varepsilon < 11.001, \\ 0.1 & \text{if } 11.001 \leq \varepsilon < 61.001, \\ 0.5 & \text{if } 61.001 \leq \varepsilon < 101.001. \end{cases} \quad (38)$$

$$\Delta n_B(\text{fm}^{-3}) = \begin{cases} 0.0005 & \text{if } 0 \leq n_B < 0.15, \\ 0.001 & \text{if } 0.15 \leq n_B < 0.3, \\ 0.01 & \text{if } 0.3 \leq n_B < 1, \\ 0.025 & \text{if } 1 \leq n_B < 5. \end{cases} \quad (39)$$

A small value for discretization is chosen to correctly reproduce the critical behavior and discontinuity in thermodynamic quantities due to the first-order transition beyond the critical point. For other values of (ε, n_B) , the pressure and other thermodynamic variables are obtained through two-dimensional linear interpolation. For all those (ε, n_B) where T and μ_B lie outside the range (5, 450) and (0, 450) MeV, respectively, the thermodynamic variables are put to zero.

D. Transport coefficients

Before providing expressions for the transport coefficients, we shall give an account of how the equilibrium correlation length is obtained from the equation of state with CP . The procedure of Ref. [41] has been followed to calculate the equilibrium correlation length, ξ , which is computed in the Ising model by taking the derivative of equilibrium magnetization, $M(r, h)$, with respect to h at fixed r as follows:

$$\xi^2 = \frac{1}{H_0} \left(\frac{\partial M(r, h)}{\partial h} \right)_r. \quad (40)$$

Here, H_0 is a dimensionful parameter to get the correct dimensions of ξ . We shall take $H_0 = 1$ in our calculations. In fact, the derivative of $M(r, h)$ with respect to h is the magnetic susceptibility (χ_M) in the Ising model, which, near a critical point, goes as $\xi^{2-\eta'}$, where the value of η' is found to be small ($\eta' \approx 0.036$). In this work, we have taken $\eta' = 0$. The equilibrium magnetization is parametrized in terms of variables R and θ as

$$M(R, \theta) = M_0 R^\beta \theta, \quad (41)$$

where R and θ are related to r and h through Eqs. (33) and (34). Now, using the identity

$$\left(\frac{\partial M}{\partial h} \right)_r = \left(\frac{\partial M}{\partial R} \right)_\theta \left(\frac{\partial R}{\partial h} \right)_r + \left(\frac{\partial M}{\partial \theta} \right)_R \left(\frac{\partial \theta}{\partial h} \right)_r, \quad (42)$$

and the expressions for $\left(\frac{\partial R}{\partial h} \right)_r$ and $\left(\frac{\partial \theta}{\partial h} \right)_r$ given in Ref. [31], we have

$$\xi^2 = \frac{M_0}{h_0} \frac{R^{\beta(1-\delta)}}{2\beta\delta\theta\tilde{h}(\theta) + (1-\theta^2)\tilde{h}'(\theta)} [1 + (2\beta - 1)\theta^2]. \quad (43)$$

Near the critical point, the transport coefficients are expected to vary with the correlation length as follows:

$$\zeta \sim \xi^3, \quad \eta \sim \xi^{0.05}, \quad \kappa_T \sim \xi. \quad (44)$$

We define the region in the $\mu_B - T$ plane bounded by the curve $\xi(\mu_B, T) = \xi_0$ as the critical region; i.e., for $\xi < \xi_0$, the transport coefficients are regular functions of T and μ_B , but for $\xi > \xi_0$, the transport coefficients must satisfy the scaling laws as defined above. It may be pointed out here that ξ_0 is a parameter which controls the size of the critical region. It has not yet been calculated from the first principles. Different values of ξ_0 have been considered in the literature; e.g., it is taken as 1 and 0.5 fm respectively in Refs. [42,43]. Here, we choose $\xi_0 = 1.75$ fm, but some results for other value of ξ_0 are also shown below. In this work, we only consider bulk viscosity (ζ) and shear viscosity (η). The critical behavior of these transport coefficients can then be modeled as

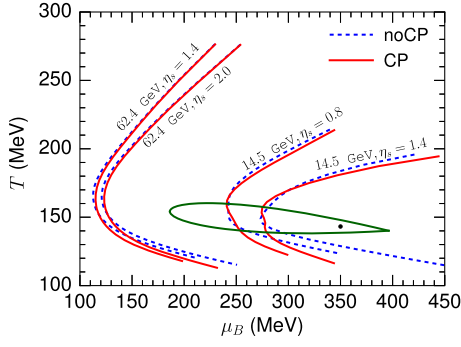


FIG. 1. Trajectories traced by the fluid cell at $x = y = 0$ in the $T - \mu_B$ plane for different space-time rapidities for two colliding energies (14.5 and 62.4 GeV) and for impact parameter $b = 5$ fm, for the purpose of illustration here. The critical point is indicated in solid black dot at $(T, \mu_B) = (350, 143.2)$ MeV, and the boundary of the critical region is indicated by the solid green line.

$$\zeta = \zeta_0 \left(\frac{\xi}{\xi_0} \right)^3, \quad \eta = \eta_0 \left(\frac{\xi}{\xi_0} \right)^{0.05}, \quad (45)$$

where ζ_0 and η_0 denote the values outside the critical region which are chosen as [38,44]

$$\eta_0(\mu_B, T) = 0.08 \left(\frac{\varepsilon + p}{T} \right),$$

$$\zeta_0(\mu_B, T) = 15\eta_0(\mu_B, T) \left(\frac{1}{3} - c_s^2 \right)^2.$$

The relaxation times in Eqs. (4) and (5) also diverge near the critical point. This is included by using the following expressions for the relaxation times of shear (τ_π) and bulk (τ_Π) viscous effects,

$$\tau_\pi = \tau_\pi^0 \left(\frac{\xi}{\xi_0} \right)^{0.05}, \quad \tau_\Pi = \tau_\Pi^0 \left(\frac{\xi}{\xi_0} \right)^3, \quad (46)$$

where τ_π^0 and τ_Π^0 are the relaxation times outside the critical region, which we take as follows (with $C_\eta = 0.08$) [44]:

$$\frac{\tau_\pi^0}{5} = \tau_\Pi^0 = \frac{C_\eta}{T}. \quad (47)$$

It may be noted here that τ_π^0 is five times larger than τ_Π^0 .

The critical domain is delineated in the $\mu_B - T$ plane by setting $\xi(\mu_B, T) = \xi_0 = 1.75$ fm. The critical point indicated by the black dot and the critical domain enclosed by the green line are shown in Fig. 1. The trajectories of the system in the $\mu_B - T$ plane formed at two $\sqrt{s_{NN}}$ with and without CP have been displayed. The trajectories of the fluid cells at lower $\sqrt{s_{NN}}$ pass through the critical region, but for higher $\sqrt{s_{NN}}$, the trajectories remain away from the critical region. But for the event-averaged initial condition

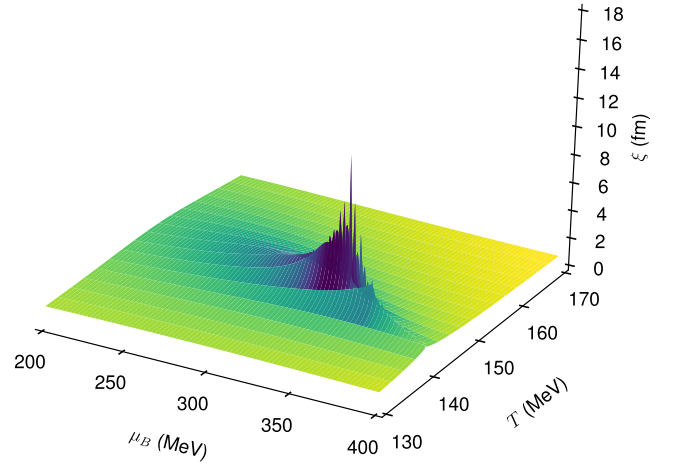


FIG. 2. Correlation length, ξ , plotted as a function of μ_B and T .

used here at fixed collision energy, the fluid cell at larger space-time rapidity, η_s , lies closer to the critical point and will feel the effect of EOS and enhanced values of transport coefficients more. In other words, the fluid cells closer to the boundary of the fireball encounter larger viscous effects induced by CP . The evolution of fluid cell at $(x, y, \eta_s) = (0, 0, 1.4)$ at $\sqrt{s_{NN}} = 14.5$ GeV is displayed in Fig. 1. The results clearly show that the trajectories at higher η_s get attracted toward the critical point. The correlation length as obtained in Eq. (43) is shown in Fig. 2 as function of μ_B and T . The drastic increase in the transport coefficients is conspicuous due to the divergent nature of the correlation length ξ .

E. Numerical implementation

We perform the hydrodynamical simulation on a $201 \times 201 \times 71$ space grid such that $\Delta x = \Delta y = \Delta \eta = 0.2$ fm. Also, the time step for the evolution is chosen as $\Delta \tau = 0.05$ fm. This choice satisfies the Courant-Friedrichs-Lewy (CFL) criterion for the stability of the code. Further, the time-evolved quantities are written to a data file after evolving for 0.5 fm time from the previous step. To prevent instabilities due to large viscosity or due to large gradients of u^μ , we follow the regularization scheme of Ref. [29], which is to rescale $\pi^{\mu\nu}$ and Π whenever they exceed a certain upper limit. As the fraction of cells encountering large viscosity is small and mostly appears toward the boundary of the fireball, this regularization scheme is not expected to change the results significantly. We use the CORNELIUS [32] code to find a constant energy density surface within a computational (fluid) cell. The CORNELIUS code provides the coordinates $(\tau_f, x_f, y_f, \eta_{sf})$ and area elements $d\Sigma_\nu$ of the freeze-out surface. The quantities like T , ε , etc. at $(\tau_f, x_f, y_f, \eta_{sf})$ are calculated through four-dimensional linear interpolation using the values at the corners of the cell. We shall analyze the effects of the CP on the surface $\varepsilon = 0.3$ GeV/fm³, henceforth denoted as Σ_{CFO} .

The aim here is not to compare and reproduce the experimental data but to pinpoint the effects that CP will induce on various hydrodynamic quantities, and hence on the experimental observables.

To calculate the space averaged quantity, say transverse velocity, $v_T = \sqrt{v_x^2 + v_y^2}$, we use the expression

$$\langle v_T \rangle(\tau) = \frac{\int d^3x \varepsilon(\tau, x, y, \eta_s) v_T(\tau, x, y, \eta_s)}{\int d^3x \varepsilon(\tau, x, y, \eta_s)}, \quad (48)$$

where $\varepsilon(\tau, x, y, \eta_s)$ is the energy density. The p_T spectrum of the hadrons, $\frac{dN}{d^2p_T dy}$, can be calculated by using the Cooper-Frye formula as

$$\frac{dN_i}{d^2p_T dy} = \frac{g_i}{(2\pi)^3} \int d\sigma_\mu p^\mu f_i(x, p), \quad (49)$$

where $f_i(x, p)$ is given by

$$f_i(x, p) = \frac{1}{e^{(p^\mu u_\mu - \mu_{B,F})/T_F} + a_i}. \quad (50)$$

Here, T_F and $\mu_{B,F}$ denote the temperature and chemical potential on the surface Σ_{CFO} , $a_i = -1$ for bosonic statistics, $a_i = +1$ for fermionic statistics, and $a_i = 0$ for classical (Boltzmann) statistics. In Sec. III, the effects of viscous correction (δf_i) to the equilibrium distribution f_i are exhibited on the elliptic flow of pions.

The other experimental measurable quantities, like flow coefficients, are calculated by using the following expression:

$$v_n(p_T, y) = \frac{\int d\phi \frac{dN}{d^2p_T dy} \cos(n\phi)}{\int d\phi \frac{dN}{d^2p_T dy}}. \quad (51)$$

The p_T -integrated flow coefficient is obtained as

$$v_n(y) = \int_{p_{T,\min}}^{p_{T,\max}} dp_T v_n(p_T, y), \quad (52)$$

where we take $p_{T,\min} = 0.2$ GeV and $p_{T,\max} = 3$ GeV. Similarly, the rapidity integrated flow coefficient is obtained as

$$v_n(p_T) = \int_{y_{\min}}^{y_{\max}} dy v_n(p_T, y), \quad (53)$$

where we have chosen $y_{\min} = -1$ and $y_{\max} = 1$.

III. RESULTS AND DISCUSSIONS

In this section, we present our results. As a test of our code, we present a comparison of our numerical results with the analytical Gubser solution in the next subsection. We have compared our results with publicly available MUSIC code and with experimental data in Ref. [28]. We also display some results from our code, with and without dissipative effects, to understand the evolution history of the system but which are not directly measured in experiments.

A. Space-time evolution of QGP

The numerical results from our code and the analytical Gubser solution are displayed in Fig. 3. The Gubser solution is given by [33,38]

$$\varepsilon(\tau, r) = \frac{\varepsilon_0}{\tau^4} \frac{(2q\tau)^{8/3}}{[1 + 2(\tau^2 + r^2) + (\tau^2 - r^2)^2]^{4/3}}, \quad (54)$$

$$n_B(\tau, r) = \frac{n_{B0}}{\tau^3} \frac{(2q\tau)^2}{[1 + 2(\tau^2 + r^2) + (\tau^2 - r^2)^2]}, \quad (55)$$

$$v_x(\tau, r) = \frac{2q^2\tau x}{1 + q^2r^2 + q^2\tau^2}, \quad (56)$$

$$v_y(\tau, r) = \frac{2q^2\tau y}{1 + q^2r^2 + q^2\tau^2}, \quad (57)$$

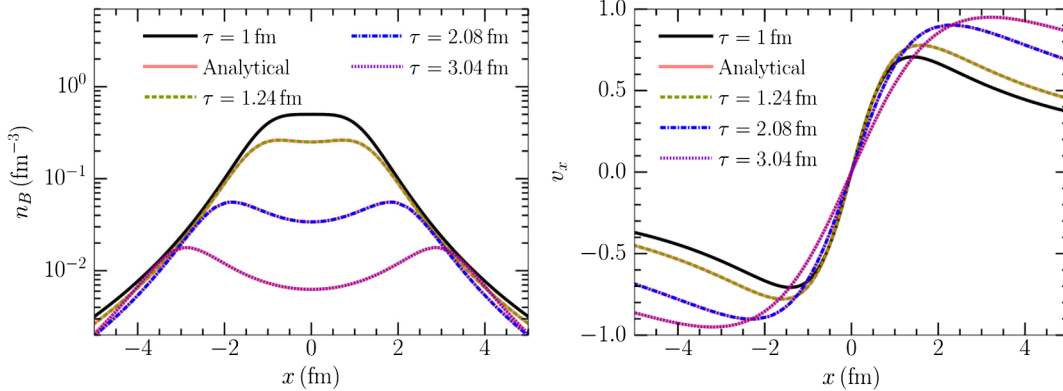


FIG. 3. Comparison of the output from our code with analytic Gubser solution. The results are plotted at $y = 0$ after setting $q = 1$ in Eqs. (55) and (56).

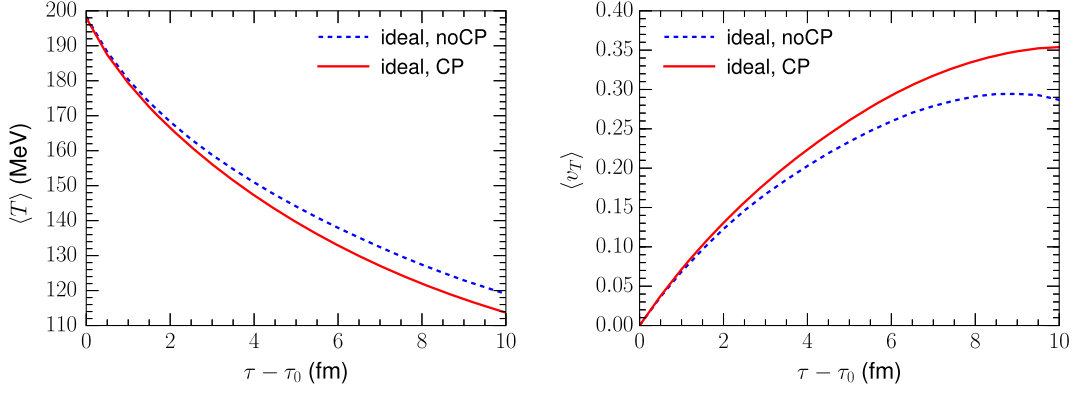


FIG. 4. Time evolution of (left) average temperature and (right) transverse velocity using ideal hydrodynamics and EOS with (*CP*, red solid line) and without (noCP, blue dashed line) the critical point for Au + Au collision at $\sqrt{s_{NN}} = 14.5$ and impact parameter $b = 5$ fm.

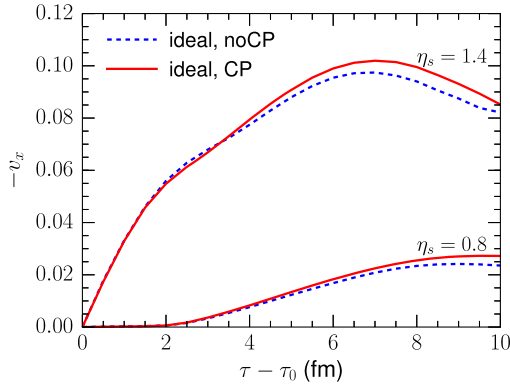


FIG. 5. Time evolution of the x component of velocity (v_x) of the fluid cell at $x = y = 0$ and at different space-time rapidities using ideal hydrodynamics for Au + Au collision at $\sqrt{s_{NN}} = 14.5$ and impact parameter $b = 5$ fm.

where $r = \sqrt{x^2 + y^2}$. The numerical solution is in perfect agreement with the analytical result. Next, we show the time evolution of the average temperature of the fireball formed in Au + Au collisions ($\sqrt{s_{NN}} = 14.5$ GeV at impact parameter $b = 5$ fm) in Fig. 4 using ideal hydrodynamics (all transport coefficients set to zero) and EOS

with (red solid line) and without (blue dashed line) the critical point.

For a given initial condition, the addition of the critical part to the regular pressure leads to a larger value of the net pressure and hence a large gradient of the pressure with respect to the vacuum outside. This leads to a faster expansion and a faster rate of cooling as shown in the left panel of Fig. 4. Higher pressure introduced by the *CP* leads to higher flow, too, as reflected in v_T , as shown in the right panel of Fig. 4.

In Fig. 5, we show the time evolution of v_x of fluid cells at two space-time rapidities for Au + Au collision at $\sqrt{s_{NN}} = 14.5$ GeV and impact parameter $b = 5$ fm. The results indicate that a gradient of v_x along the η_s direction is generated, which is due to our choice of shifted initial condition. The presence of *CP* marginally increases this gradient.

Similarly, the transverse and longitudinal expansions with averaged initial condition also increase marginally due to the presence of the critical point for ideal hydrodynamics as shown in Fig. 6. It should, however, be noted that the profile is mostly monotonic.

Now, we discuss results with the inclusion of the viscous effects in the QGP fluid. As the viscous fireball of QGP

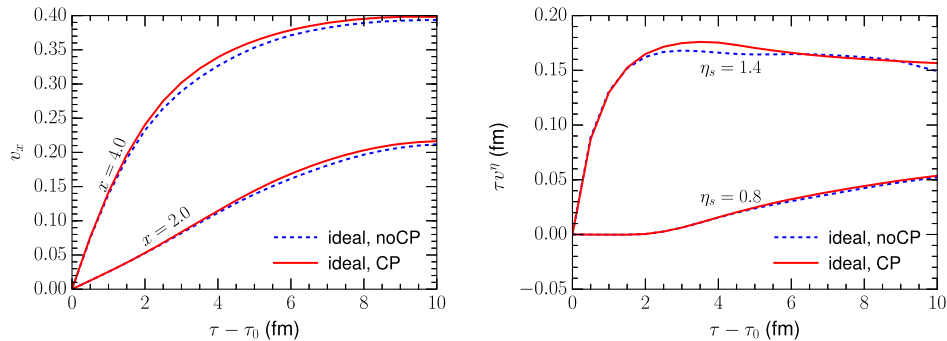


FIG. 6. Time evolution of v_x (left) for the fluid cell at $y = 0, \eta_s = 0$ at different x and time evolution of v_η (right) for the fluid cell at $x = y = 0$ at different space-time rapidities for Au + Au collision at $\sqrt{s_{NN}} = 14.5$ and impact parameter $b = 5$ fm.

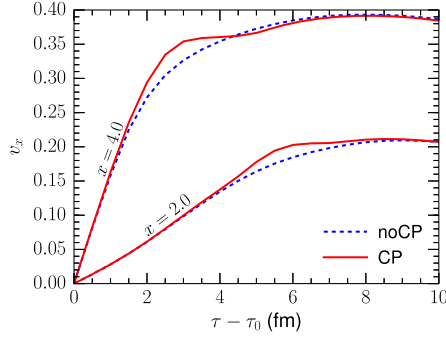


FIG. 7. Time evolution of v_x at different x for the fluid cell at $y = 0$, $\eta_s = 0$ for $\sqrt{s_{NN}} = 14.5$ GeV and $b = 5$ fm.

expands, the fluid cells toward the boundary, which are closer to the critical region, undergo slower expansion due to enhanced viscosity. The expansion of the fluid cells in the bulk is not strongly affected by the critical point. This leads to the buildup of matter somewhere in between, due to which the expansion results in a nonmonotonic profile for the initial condition used here. This is reflected in

the variation of v_x with τ for different values of x (Fig. 7) and η_s (left panel of Fig. 8). The variation of τv_η with τ for different values of η_s displays similar nature (right panel of Fig. 8). The nonmonotonicity is prominent for larger values of η_s , which corresponds to the evolution trajectory closer to the CP (see Fig. 1). The effect of CP on v_x at $\eta_s = 1.4$ gives rise to a hornlike structure. We will check below whether such structure survives in the space-time integrated observables. It is to be stressed further that as the critical point is approached these effects get enhanced. To further confirm this argument, we also show the velocity profile for $\sqrt{s_{NN}} = 62.4$ GeV in Fig. 9. The trajectories in this case are far away from the critical region, and thus the effects of EOS and enhanced viscosities are small. Therefore, the nonmonotonicity observed in the time evolution of v_x and τv_η can be attributed to the CP . However, it will be interesting to examine whether such effects of CP survive in experimental observables like p_T spectra and various flow coefficients which are obtained by integrating over the entire space-time history of the fireball. This exercise has been carried out below.

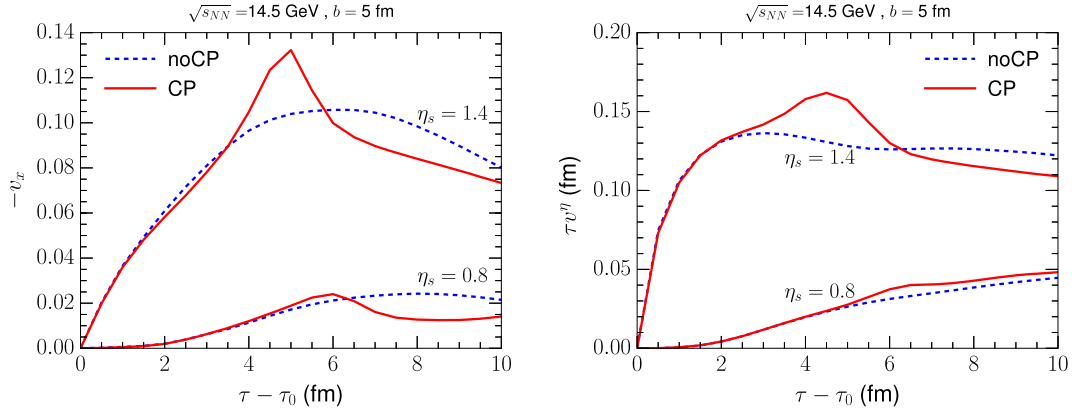


FIG. 8. Time evolution of v_x at different values of x (left panel) and τv_η at different η_s for the fluid cell at $x = y = 0$, for $\sqrt{s_{NN}} = 14.5$ GeV and $b = 5$ fm.

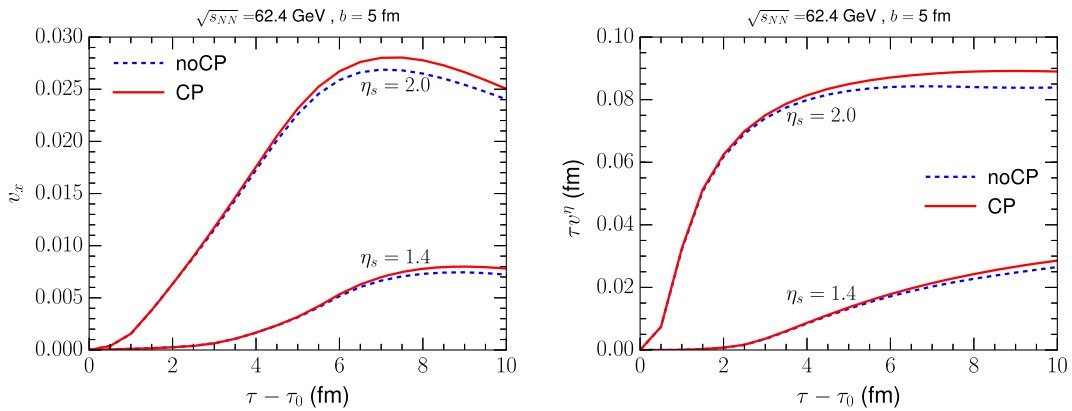


FIG. 9. Same as Fig. 8 for $\sqrt{s_{NN}} = 62.4$ GeV.

B. Effects of CP on the spectra and flow coefficients

In this subsection, we display the effects of CP on quantities which are commonly measured in experiments. These quantities are the p_T spectra and directed and elliptic flow coefficients of pion and proton, which are estimated by including the effects of CP on the EOS and transport coefficients. The p_T spectra of π^+ and proton are displayed in Fig. 10 for two colliding energies, i.e., $\sqrt{s_{NN}} = 14.5$ (left panel) and 62.4 GeV (right panel). The rapidity distribution of the pion and proton are shown in Fig. 11 for two colliding energies, i.e., $\sqrt{s_{NN}} = 14.5$ GeV and $\sqrt{s_{NN}} = 62.4$ GeV; no distinguishable effect of CP is found. The results displayed in Fig. 11 demonstrate the change in dN/dy due to differential change in viscosities induced by CP . The fluid cells toward the boundary of the fireball, which are closer to the CP , encounter larger dissipation compared to fluid cells in the bulk. On the other hand, the gradient of pressure becomes steeper due to the addition of critical contribution to pressure. This results in matter being pushed from the bulk toward the boundary, for example, from midrapidity to forward rapidity. This suggests that the

entropy density is carried away from midrapidity, resulting in a decrease of dN/dy around midrapidity and a corresponding increase at forward rapidity. These effects are clearly visible when the simulation is performed in 1 + 1 dimensions (Ref. [41]). However, in the present (3 + 1)-dimensional case, the increase in forward rapidity might not even be visible due to the tiny fraction of cells encountering enhanced viscosity at the fireball boundary. Consequently, we observe a slight decrease in dN/dy at all rapidities. Moreover, the effects of CP on the spectra are found to be insignificant because both the p_T and y distributions are obtained by integration over the space-time evolution history of the fireball produced in these collisions; i.e., results are a superposition of all the temperatures and densities through which the system passes, and results do not depend on the point (μ_{BC}, T_c) alone.

The rapidity distribution of v_1 of the proton and pion are displayed in Fig. 12 as a function of y for $\sqrt{s_{NN}} = 14.5$ and 62.4 GeV. The effects of CP on both π^+ and the proton are seen to be insignificant as expected. The elliptic flow of both protons and π^+ increases marginally around $p_T \sim 2$ GeV

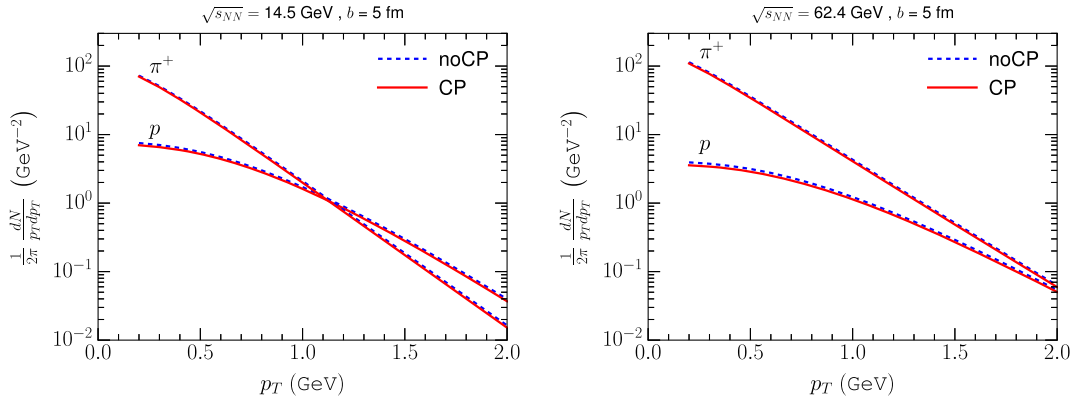


FIG. 10. Transverse momentum spectra of π^+ and proton are obtained by integrating over ϕ and rapidity (y) (for $-1 \leq y \leq 1$ for $\sqrt{s_{NN}} = 14.5$ (left panel) and 62.4 GeV (right panel)).

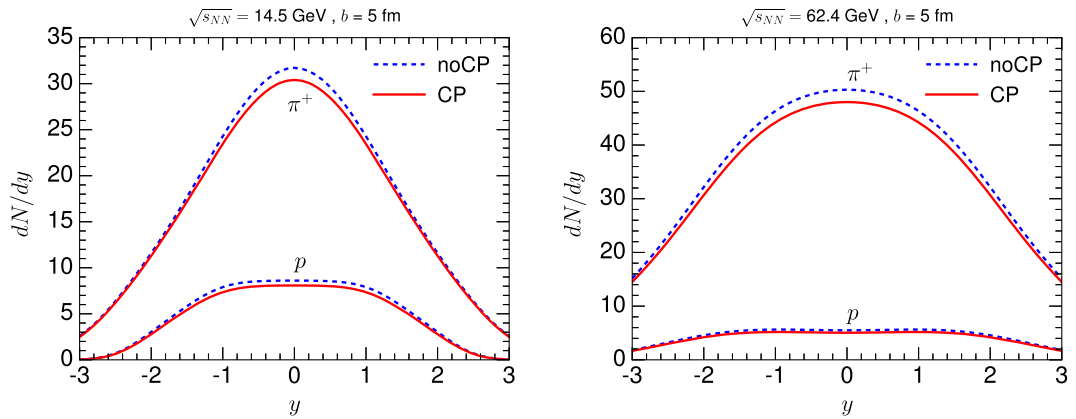


FIG. 11. The rapidity distribution of pion and proton for $\sqrt{s_{NN}} = 14.5$ (left panel) and 62.4 GeV (right panel).

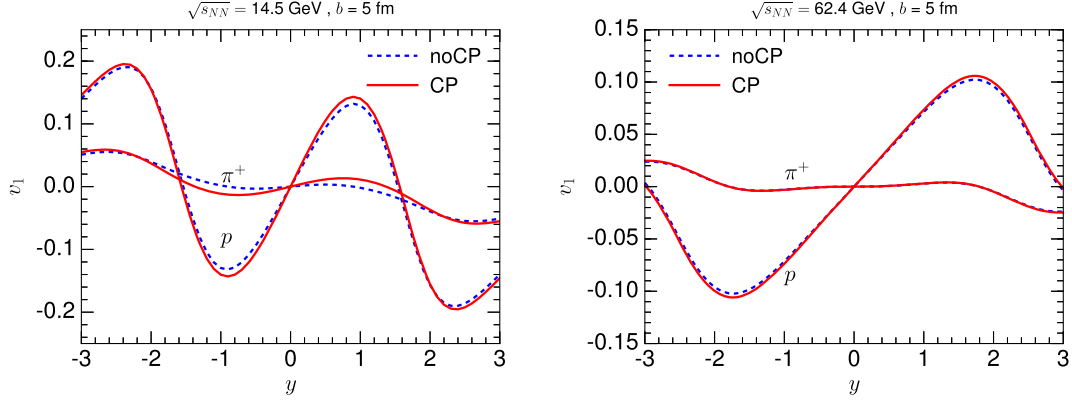


FIG. 12. Rapidity dependence of directed flow for two colliding energies, 14.5 (left) and 62.4 GeV (right) for $b = 5$ fm.

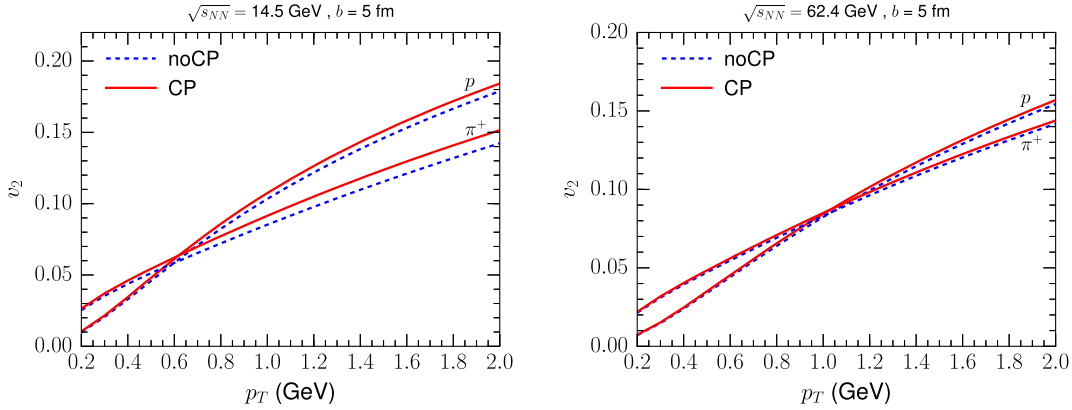


FIG. 13. The p_T dependence of elliptic flow for two colliding energies, 14.5 (left) and 62.4 GeV (right) for $b = 5$ fm.

compared to the case when there is no CP (left panel of Fig. 13) for $\sqrt{s_{NN}} = 14.5$ GeV. For $\sqrt{s_{NN}} = 62.4$ GeV, there is no shift in v_2 due to the inclusion of CP (right panel of Fig. 13), which is expected because the trajectory in this case remains away from the critical domain.

A faster expansion leads to a rapid fall in temperature and chemical potential, which leads to a slight reduction in the yield of both π^+ and protons as shown in Fig. 10. These effects will definitely get enhanced as we approach the critical point. However, within the current model, the effect is only marginal and might not even be detected experimentally. As has been shown in Ref. [28], the thermal vorticity which depends on the velocity gradient of the fluid is suppressed by the presence of CP . Consequently, the rapidity dependence of the spin polarization of the Λ hyperon was shown to be drastically affected by the CP due to the coupling of the spin with the thermal vorticity. The CP may be detected by measuring the rapidity distribution of the spin polarization by tuning the beam energy. Therefore, one expects that those observables which depend on the gradient of velocity to be efficient signatures of the CP .

Next, we study the sensitivity of some of the results on the critical domain size, determined by the value of ξ_0

and on the viscous corrections to phase-space distribution function. The results displayed below are obtained for $\sqrt{s_{NN}} = 14.5$ GeV. In Fig. 14, the multiplicity distribution of π^+ as a function of rapidity is depicted for $\xi_0 = 1.75$ and 1.2 fm. The ξ_0 dependence of η ($\propto (\xi/\xi_0)^{0.05}$) and ζ ($\propto (\xi/\xi_0)^3$) indicates that the dissipation increases with the decrease in ξ_0 . This leads to the reduction of multiplicity due to enhanced dissipation confronted by the system.

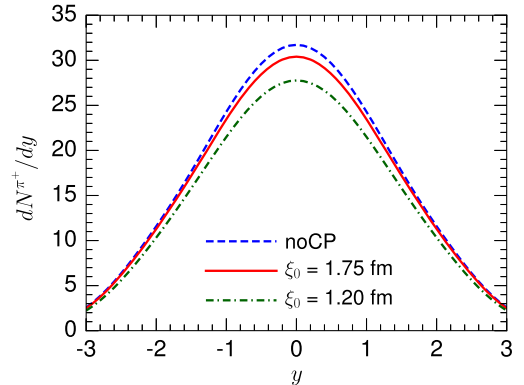


FIG. 14. The variation of multiplicity with rapidity for different values of ξ ($\xi_0 = 1.75$ and 1.2 fm) at $\sqrt{s_{NN}} = 14.5$ GeV.

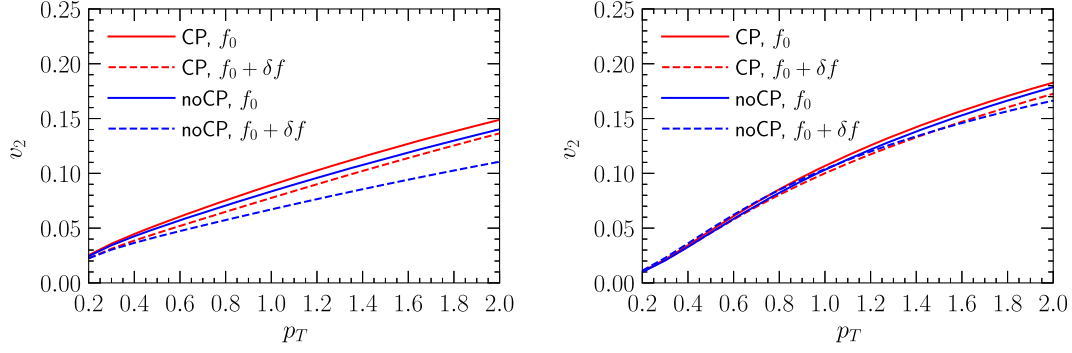


FIG. 15. The variation of elliptic flow of pions (left panel) and proton (right panel) with transverse momentum is displayed at $\sqrt{s_{NN}} = 14.5$ GeV with the inclusion of viscous correction to the phase-space distribution for $\xi_0 = 1.75$ fm. δf denotes viscous correction to the equilibrium distribution function.

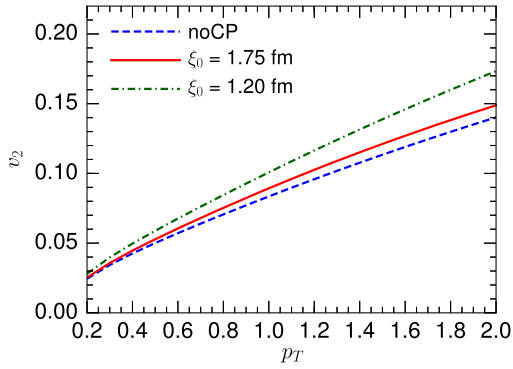


FIG. 16. The elliptic flow of pions is shown as a function of transverse momentum at $\sqrt{s_{NN}} = 14.5$ GeV for $\xi_0 = 1.75$ and 1.2 fm.

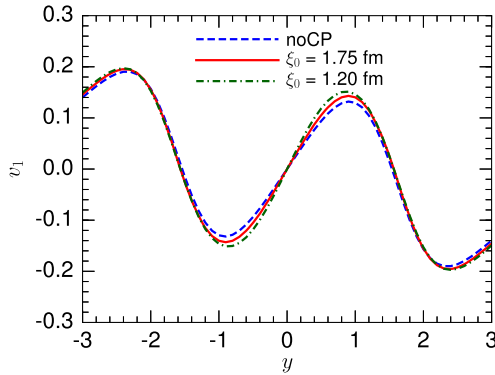


FIG. 17. The variation of directed flow with rapidity at $\sqrt{s_{NN}} = 14.5$ GeV for $\xi_0 = 1.75$ and 1.2 fm.

We have estimated the elliptic flow of pion with viscous correction to equilibrium phase space distribution, δf [38]. It is found that v_2 reduces due to viscous correction and the reduction is more at higher p_T (Fig. 15) as found in Ref. [38] also. The effects of δf on v_2 of the proton are found to be smaller than that of the pion. For smaller ξ_0 , the elliptic flow of pions is found to be

larger (Fig. 16), whereas the effect on directed flow is negligible (Fig. 17).

IV. SUMMARY AND DISCUSSIONS

We have developed a computer code to solve the relativistic viscous causal hydrodynamics in $(3 + 1)$ dimensions. The effects due to the QCD critical point have been included in the code through the equation of state and scaling behavior of the transport coefficients. We study the evolution of the fireball of quarks and gluons formed at two colliding energies, $\sqrt{s_{NN}}$. The p_T spectra and directed and elliptic flow coefficients of pions and protons have been evaluated to understand the effects of CP on these quantities. We find that the integration over the entire space-time history of the fireball mostly wipes out the effects of CP on the spectra and flow coefficients, which indicates that the detection of CP by using the hadronic spectra may not be useful. The effects of viscous corrections to equilibrium distribution functions have been estimated and found to be negligible on the p_T spectra of hadrons and directed flow. However, a non-negligible effect of δf on v_2 is seen at higher p_T . However, it is shown in Ref. [28] that the CP has the potential to substantially alter the rapidity distribution of spin polarization of hadrons; therefore, the measurement of spin polarization as a function of rapidity can be considered as an efficient tool to detect the CP .

Some comments on the scope of extension of the present work are discussed below. It is well known that the fluid dynamics becomes invalid near the CP because the fluctuating modes do not relax faster than the time-scale of changes in slow/conserved variables due to which the local thermal equilibrium cannot be maintained. However, the results obtained in this work may be considered reasonable because of the following reasons. First, the validity of the fluid dynamics can be extended by adding a scalar field representing the slow nonhydrodynamic modes connected to the relaxation rate of the critical fluctuation (see Refs. [45,46] for details).

In a simple picture describing the evolution of a system near the CP , it has been explicitly shown that the modes associated with the scalar fields lag behind the hydrodynamic modes, resulting in backreactions on the hydrodynamic variables; however, it was found that the backreaction has negligible effects on the hydrodynamic variables [42]. Second, one may recall that if a system is not too close to CP then hydrodynamics can still be applied in a domain around the CP [47]. Regardless of these arguments, the investigation of the effect of the scalar field on (3 + 1)-dimensional hydrodynamic evolution near the CP will be useful for future study in its own right.

In the present work, the EOS is obtained by mapping the 3D Ising model in (r, h) plane to the QCD in (μ_B, T) plane,

as they belong to the same universality class [31]. It is assumed here that both the chemical potentials corresponding to strangeness (μ_s) and electric charge (μ_Q) are zero. However, this mapping cannot be used if $\mu_Q \neq 0$ and $\mu_s \neq 0$ (constrained by strangeness neutrality [48]). The roles of μ_s and μ_Q on the EOS near CP are ignored here for simplicity, although they may have interesting effects on the critical behavior of the system.

In this work, the hydrodynamic equations are solved for event averaged (nonfluctuating) initial condition. Under these conditions, the effects of CP on the transverse momentum spectra and flow coefficients are not significant. However, the signature of CP through these observables may emerge for an event-by-event fluctuating initial condition, which we leave to future work.

-
- [1] A. Bazavov, F. Karsch, S. Mukherjee, and P. Petreczky (USQCD Collaboration), *Eur. Phys. J. A* **55**, 194 (2019).
 - [2] Z. Fodor and S. D. Katz, *J. High Energy Phys.* 03 (2002) 014.
 - [3] M. Asakawa and K. Yazaki, *Nucl. Phys.* **A504**, 668 (1989).
 - [4] A. M. Halasz, A. D. Jackson, R. E. Shrock, M. A. Stephanov, and J. J. M. Verbaarschot, *Phys. Rev. D* **58**, 096007 (1998).
 - [5] P. de Forcrand and O. Philipsen, *Nucl. Phys.* **B642**, 290 (2002).
 - [6] Y. Aoki, G. Endrődi, Z. Fodor, S. D. Katz, and K. K. Szabó, *Nature (London)* **443**, 675 (2006).
 - [7] V. Dexheimer, J. Noronha, J. Noronha-Hostler, N. Yunes, and C. Ratti, *J. Phys. G* **48**, 073001 (2021).
 - [8] G. Endrődi, Z. Fodor, S. D. Katz, and K. K. Szabó, *J. High Energy Phys.* 04 (2011) 001.
 - [9] Z. Fodor and S. D. Katz, *J. High Energy Phys.* 04 (2004) 050.
 - [10] H.-T. Ding, F. Karsch, and S. Mukherjee, *Int. J. Mod. Phys. E* **24**, 1530007 (2015).
 - [11] R. V. Gavai, *Pramana* **84**, 757 (2015).
 - [12] P. Deb, A. Bhattacharyya, S. K. Ghosh, R. Ray, and A. Lahiri, *Nucl. Phys.* **A862–863**, 267 (2011).
 - [13] B.-J. Schaefer, J. M. Pawłowski, and J. Wambach, *Phys. Rev. D* **76**, 074023 (2007).
 - [14] T. K. Herbst, J. M. Pawłowski, and B.-J. Schaefer, *Phys. Lett. B* **696**, 58 (2011).
 - [15] J. Wambach, B.-J. Schaefer, and M. Wagner, *Acta Phys. Pol. Suppl. Ser. 3*, 691 (2010), <https://www.actaphys.uj.edu.pl/S/3/3/691>.
 - [16] O. DeWolfe, S. S. Gubser, and C. Rosen, *Phys. Rev. D* **83**, 086005 (2011).
 - [17] D. Mroczek, A. R. Nava Acuna, J. Noronha-Hostler, P. Parotto, C. Ratti, and M. A. Stephanov, *Phys. Rev. C* **103**, 034901 (2021).
 - [18] M. A. Stephanov, K. Rajagopal, and E. V. Shuryak, *Phys. Rev. Lett.* **81**, 4816 (1998).
 - [19] T. Dore, J. M. Karthein, I. Long, D. Mroczek, J. Noronha-Hostler, P. Parotto, C. Ratti, and Y. Yamauchi, *Phys. Rev. D* **106**, 094024 (2022).
 - [20] X. Luo and N. Xu, *Nucl. Sci. Tech.* **28**, 112 (2017).
 - [21] J. Brewer, S. Mukherjee, K. Rajagopal, and Y. Yin, *Phys. Rev. C* **98**, 061901 (2018).
 - [22] M. A. Stephanov, *Phys. Rev. Lett.* **102**, 032301 (2009).
 - [23] M. A. Stephanov, *Phys. Rev. Lett.* **107**, 052301 (2011).
 - [24] Y. Yin, [arXiv:1811.06519](https://arxiv.org/abs/1811.06519).
 - [25] P. Romatschke and U. Romatschke, *Relativistic Fluid Dynamics In and Out of Equilibrium*, Cambridge Monographs on Mathematical Physics (Cambridge University Press, Cambridge, England, 2019).
 - [26] C. Shen and L. Yan, *Nucl. Sci. Tech.* **31**, 122 (2020).
 - [27] W. Israel and J. M. Stewart, *Ann. Phys. (N.Y.)* **118**, 341 (1979).
 - [28] S. K. Singh and J. Alam, [arXiv:2110.15604](https://arxiv.org/abs/2110.15604).
 - [29] I. Karpenko, P. Huovinen, and M. Bleicher, *Comput. Phys. Commun.* **185**, 3016 (2014).
 - [30] C. Shen and S. Alzhrani, *Phys. Rev. C* **102**, 014909 (2020).
 - [31] P. Parotto, M. Bluhm, D. Mroczek, M. Nahrgang, J. Noronha-Hostler, K. Rajagopal, C. Ratti, T. Schäfer, and M. Stephanov, *Phys. Rev. C* **101**, 034901 (2020).
 - [32] P. Huovinen and H. Petersen, *Eur. Phys. J. A* **48**, 171 (2012).
 - [33] S. S. Gubser, *Phys. Rev. D* **82**, 085027 (2010).
 - [34] P. F. Kolb, J. Sollfrank, and U. W. Heinz, *Phys. Rev. C* **62**, 054909 (2000).
 - [35] B. Schenke, S. Jeon, and C. Gale, *Phys. Rev. C* **82**, 014903 (2010).
 - [36] J. R. Cudell, V. V. Ezhela, P. Gauron, K. Kang, Y. V. Kuyanov, S. B. Lugovsky, E. Martynov, B. Nicolescu, E. A. Razuvaev, and N. P. Tkachenko (COMPETE Collaboration), *Phys. Rev. Lett.* **89**, 201801 (2002).
 - [37] B. Abelev *et al.* (ALICE Collaboration), *Phys. Rev. C* **88**, 044909 (2013).
 - [38] G. S. Denicol, C. Gale, S. Jeon, A. Monnai, B. Schenke, and C. Shen, *Phys. Rev. C* **98**, 034916 (2018).

- [39] S. Ryu, V. Jupic, and C. Shen, *Phys. Rev. C* **104**, 054908 (2021).
- [40] D. H. Rischke, Y. Pürsün, and J. A. Maruhn, *Nucl. Phys. A* **595**, 383 (1995).
- [41] A. Monnai, S. Mukherjee, and Y. Yin, *Phys. Rev. C* **95**, 034902 (2017).
- [42] K. Rajagopal, G. Ridgway, R. Weller, and Y. Yin, *Phys. Rev. D* **102**, 094025 (2020).
- [43] M. Pradeep, K. Rajagopal, M. Stephanov, and Y. Yin, *Phys. Rev. D* **106**, 036017 (2022).
- [44] G. S. Denicol, S. Jeon, and C. Gale, *Phys. Rev. C* **90**, 024912 (2014).
- [45] M. Stephanov and Y. Yin, *Nucl. Phys. A* **967**, 876 (2017).
- [46] M. Stephanov and Y. Yin, *Phys. Rev. D* **98**, 036006 (2018).
- [47] H. E. Stanley, *Introduction to Phase Transitions and Critical Phenomena*, International Series of Monographs on Physics (Oxford University Press, 1971).
- [48] J. M. Karthein, D. Mroczek, A. R. Nava Acuna, J. Noronha-Hostler, P. Parotto, D. R. P. Price, and C. Ratti, *Eur. Phys. J. Plus* **136**, 621 (2021).